Available online at www.sciencedirect.com

ScienceDirect

Procedia Structural Integrity 7 (2017) 116–123

Structural Integrity Procedia

www.elsevier.com/locate/procedia

3rd International Symposium on Fatigue Design and Material Defects, FDMD 2017, 19-22 September 2017, Lecco, Italy

Fatigue properties of Ti6Al4V cellular specimens fabricated via SLM: CAD vs real geometry

M.Dallago[a]*, V. Fontanari[a], B. Winiarski[b,c], F. Zanini[d], S. Carmignato[d], M. Benedetti[a]

[a]*Department of Industrial Engineering, University of Trento, Via Sommarive, 9, Trento 38123, Italy*
[b]*Thermo Fisher Scientific (FEI Czech Republic s.r.o) Vlastimila Pecha 12, Brno 627 00, Czech Republic*
[c] *Henry Moseley X-ray Imaging Facility, School of Materials, University of Manchester, Manchester, M13 9PL, U.K.*
[d]*University of Padova, DTG, Stradella San Nicola 3, Vicenza, Italy*

Abstract

Fully dense titanium alloy implants have long been used for the replacement and stabilization of damaged bone tissue. Nevertheless, they can cause stress shielding which brings to a loss of bone mass. Additive manufacturing (AM) allows obtaining highly porous cellular structures with a wide range of cell morphologies to tune the mechanical properties to match that of the patient's bone. In this work, the fully reversed fatigue strength of cellular specimens produced by Selective Laser Melting (SLM) of Ti-6Al-4V alloy was measured. Their structures are determined by cubic cells packed in six different ways and their elastic modulus is roughly 3GPa to match that of trabecular bone. Part of the specimens was left as sintered and part treated by Hot Isostatic Pressing (HIP). The fatigue resistance of such AM parts can be affected by surface morphology, geometrical accuracy as well as internal defects. Micro X-ray computed tomography (CT) was used in this work to compare the geometry of the produced specimens with the CAD model and to carry out residual stress measurements using the Plasma FIB-SEM-DIC micro-hole drilling method.

Peer-review under responsibility of the Scientific Committee of the 3rd International Symposium on Fatigue Design and Material Defects.

Keywords: cellular materials; SLM; fatigue; computed tomography; defects

* Corresponding author.
E-mail address: michele.dallago@unitn.it

Peer-review under responsibility of the Scientific Committee of the 3rd International Symposium on Fatigue Design and Material Defects.
10.1016/j.prostr.2017.11.068

1. Introduction

Nowadays, metals are the best choice for load bearing biomedical implants (Ryan, 2006) and Ti alloys are in general preferred to other metals such as stainless steel and Co-alloys because of their high resistance and stiffness to weight ratio and good corrosion resistance (Long, 1998; Murr, 2010). In addition, they are biocompatible (Rack, 2006). Ti6Al4V is the most popular Ti alloy because of a good combination of strength and ductility (Rack, 2006). Traditional fully dense implants can cause stress-shielding which brings to a loss of bone mass. The most used approach to avoid this negative phenomenon is to reduce the stiffness of the implant (Tan, 2017). With the advent of additive manufacturing (AM) it became possible to obtain materials with a highly porous cellular structure characterized by a wide range of cell morphologies that allow to finely tune the mechanical properties to match that of the patient's bone (Zhao, 2016a). Among the various AM techniques, Selective Laser Melting (SLM) allows greater precision (Tan, 2017) and is employed to produce the specimens object of this study.

AM metallic artefacts present numerous defects in terms of pores and surface roughness (Khademzadeh, 2016). Pores in SLM products are generally irregular (Zhao, 2016b). Irregular pores are mainly due to incomplete melting of the precursor particles, while spherical pores are due to trapped gases (Zhao, 2016b). The latter are more difficult to close via HIP (Qiu, 2013). Some pores are also carried over from the precursor powder (Qiu, 2013). In addition, geometric irregularities are typically also present as non-uniform cell wall thickness along its length and strut waviness (Zargarian, 2016). Unmelted and partly melted powder particles in the proximity of the melt can become attached to the surface, greatly increasing the surface irregularity (Zhao, 2016b).

Fatigue resistance is a critical aspect when load bearing biomedical implants are considered (Zhao 2016b). Ti-alloys in general have high notch sensitivity (Long, 1998; Niinomi, 2008), so fatigue resistance is strongly influenced by defects that act as stress raisers (Leuders, 2013; de Krijger, 2016). Leuders (2013) observed that pores are detrimental for fatigue crack initiation, while tensile residual stresses are detrimental for fatigue crack propagation. Thus, fatigue resistance of Ti6Al4V porous AM structures can be improved by HIP treatment because porosity is reduced (Leuders, 2013) and the microstructure is improved (ductile $\alpha+\beta$ phase) (Van Hooreweder, 2017). It is important to stress that the unit cell relative density and morphology are decisive regarding the mechanical behavior of the whole structure (Ahmadi, 2015; Zhao 2016b).

The paper presents the results of the fatigue and dimensional characterization of different regular open-cell cellular structures produced by SLM of Ti6Al4V alloy. Six different configurations of the cubic cell were chosen: in three of them the cubes are simply shifted to fill the 3D space, while in the other three the cubic cells are skewed to obtain structures with a cylindric symmetry. Each specimen was provided with threaded heads to carry out fully reversed fatigue tests. Micro X-ray computed tomography (CT) was used to measure these specimens as it is an advanced technique that can effectively perform non-destructive evaluations of AM components characterized by inner geometries and internal porosity, including cellular specimens (Wits, 2016; Kerckhofs, 2008). Moreover, μCT systems specifically developed for coordinate metrology are currently available to perform accurate dimensional and geometrical analyses (De Chiffre, 2014). The specimens were scanned with two different μCT systems: (i) a metrological micro CT system to perform an extensive dimensional analysis for assessing the quality of the manufacturing process and the discrepancy between the actual measured cell parameters and the nominal CAD values and (ii) a helical scanning trajectory μCT system to locate a region of interest where residual stresses were measured using the Plasma FIB-SEM-DIC micro-hole drilling method (Winiarski, 2016). Half of the specimens was subjected to HIP and the effect of this treatment on porosity and the mechanical properties was also investigated.

2. Materials and methods

2.1. Cellular specimens

Six different open-cell cellular structures were considered in this work, shown in Figure 1a: regular cubic cells (CUB-NS), single staggered cubic cells (CUB-S), double staggered cubic cells (CUB-2S), regular cylindrical cells (CYL-R), single staggered cylindrical cells (CYL-S) and double staggered cylindrical cells (CYL-2S). All the structures were designed with care in eliminating every sharp notch. The cross-section of the cell walls is thus circular and all the junctions are filleted with the same nominal radius. These structures are intended to be employed

in the production of fully porous orthopedic implants and were designed using the Finite Elements method to obtain an elastic modulus of roughly 3 GPa to match that of trabecular bone. The specimens were additively manufactured via SLM starting from the biomedical Ti grade Ti6Al4V ELI (Grade 23) in form of powder of mean diameter of 8.64 μm (Figure 1b). The specimens were built along a direction inclined 45° to the longitudinal one using a 3D System ProX DMP 300 printer. Further details are provided in Benedetti (2017). The specimens were divided into two batches. The first was heat treated at 670° C for 5 hours in Ar protective atmosphere to relieve residual stresses (referred to as "as-built"), the second was treated by HIP at 920° C and 1000 bar for 2 hours (referred to as "HIPed").

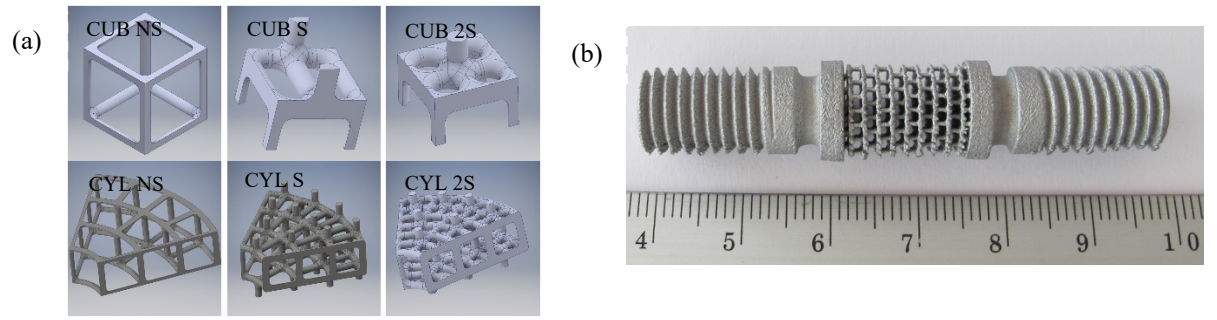

Figure 1. (a) CAD models of the six cellular structures studied; (b) example of specimen with the threaded heads for push-pull fatigue tests.

The geometrical parameters that characterize each cell are the cell wall length L, the cell wall diameter t_0 and the fillet radius R at the junctions and are reported in Table 1 together with the elastic modulus calculated via FE method form the CAD models.

Table 1. CAD geometrical parameters of the cellular structures and effective elastic modulus (from FE applied to the CAD models).

Structure	t_0 (mm)	R (mm)	FE elastic modulus (MPa)	Relative density (%)
CUB-NS	0.260	0.130	3021	6.61
CUB-S	0.340	0.170	3220	15.32
CUB-2S	0.350	0.175	3208	19.61
CYL-NS	0.230	0.115	3000	6.04
CYL-S	0.300	0.150	2960	12.39
CYL-2S	0.350	0.175	2480	18.39

2.2. Porosity analysis

To measure the porosity and the dimensional parameters, two sections were cut from each specimen: a transversal and a longitudinal with respect to the loading direction. The sectioned samples are then mounted, ground using SiC abrasive papers (with 120, 180, 320, 400, 600, 1000, 1500 grit sizes), and polished using a 3-micron diamond paste and a 0.04-micron alumina suspension. Pores were counted and their area measured on each section using image analysis software ImageJ®. The maximum pore size in the whole specimen is estimated from the distribution of the pore sizes on the analyzed section with a statistical approach based on the statistics of extreme values, as described in Beretta (1998) and Murakami (2002).

2.3. CT dimensional evaluation

The central cellular part of one specimen for each type (see Section 2.1) was scanned using a metrological CT system (Nikon Metrology MCT225) characterized by micro-focus X-ray tube, 16-bit detector with 2000×2000 pixels, high-precision linear guideways and controlled cabinet temperature (20±0.2 °C). The voxel size (i.e. the size of the volumetric pixel) of the reconstructed three-dimensional models was equal to 8.3 μm. In this work, a new Matlab (MathWorks, USA) routine was implemented to identify the spatial coordinates of nodes using a high-

density point cloud extracted from the CT scanned volumes. The actual position of nodes was then compared with their nominal position. The cell-wall diameter distribution of the cellular structures was evaluated using the evaluation software VGStudio MAX 3.0 (Volume Graphics GmbH, Germany) and was then compared with the nominal diameter.

2.4. Residual stress measurement using the micro-hole drilling method

The residuals stresses in an as-built CUB-NS specimen were measured using a Plasma FIB-SEM-DIC micro-hole drilling method (Winiarski, 2016). In order to locate a suitable region of interest for the stress measurements the scaffold was scanned using FEI HeliScan^{TM} μCT scanner (800 nm resolution using 2D JIMA resolution test). The achieved voxel size was $(4.8\ \mu m)^3$ in this case. After 3D reconstruction of the scaffold, a suitable region of interest was selected near a junction, A, to measure residual stress in the circumferential and axial direction of the strut shown in Figure 2. Later, a portion of material was removed near the junction (Figure 2c) to create flat and smooth surface needed for reliable measurements with micro-hole drilling method. PFIB was used at 30 kV/1.3 μA for about 3 hours of continuous milling. Next an array of submicron-holes (diameter ~400-800 nm) were milled PFIB using a bitmap file with predefined random pattern. The submicron-holes work in a similar way as Pt nano-dots, thus enhance the topological contrast of FEGSEM imaging and improve the accuracy of DIC displacement/strain measurement (Winiarski, 2012a). Two micro-holes of 20 μm diameter and 10 μm deep (1 and 2 in Figure 2d) were milled (15 nA at 30 kV). The dimensions of the holes were selected so that the surface topography (roughness) after site preparation is much smaller than the micro-hole dimensions. In the stress mapping process, a sequence of three FEGSEM images (dwell time, Dt = 3μs, 8 frames averaged, ETD detector) of the patterned areas were acquired at 0° stage tilt before and three images after milling. The theoretical concepts on which the calculation of the residual stresses is based and the related procedure are reported in Schajer (2013) and Winiarski (2012b).

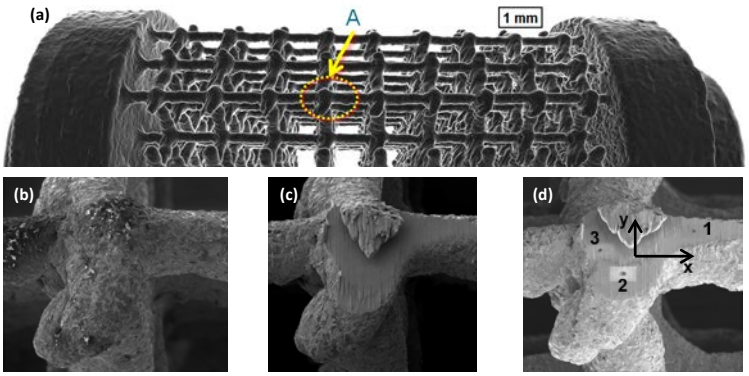

Figure 2. Position of residual stress measurements with the micro-hole drilling method on a CUB-NS specimen; a) shows volume rendered of reconstructed micro CT projections, where A indicates the measurements location, b) and c) shows the junction before and after preparation for the measurements, d) shows locations of micro-holes 1 and 2, while micro-hole 3 is used for testing milling conditions before actual measurements.

2.5. Fatigue testing

Axial fatigue tests were carried out in laboratory environment using a RUMUL Mikrotron 20 kN resonant testing machine equipped with a 1 kN load cell operating at a nominal frequency of 120 Hz under load control. The specimens were subjected to constant amplitude fully reversed fatigue cycles (zero mean stress, $R = -1$). The fatigue resistance at 10^6 cycles of the different structures has been estimated according to a step loading procedure developed by Maxwell (1999) for Ti alloys that considerably reduces the testing time and the amount of expensive experimental material with respect to standard methods. A sample of three specimens was tested for each structure, for a total of 18 specimens. The fatigue notch factor K_f and the stress concentration factor K_t were also calculated

with Eqs. 1 and 2, respectively:

$$K_f = \frac{\text{fatigue resistance of bulk specimen}}{\text{fatigue resistance of the cellular specimen}} \quad (1)$$

$$K_t = \frac{\text{maximum von Mises equivalent stress in the structure}}{\text{nominal homogeneous stress}} \quad (2)$$

The nominal homogeneous stress and the fatigue resistance of the cellular specimens were calculated by dividing the force applied to the cellular structure by its nominal cross section (i.e. the section measured as if the cellular material was a bulk material).

3. Results and discussion

3.1. Porosity analysis

The estimated maximum defect size measured as $\sqrt{area}_{\max}$ (Beretta, 1998) for each structure is shown in Figure 3. It is possible to note how HIPing is effective in reducing the size of the biggest pores. The cylindrical specimens are richer in pores than the cubic ones, this is most likely because the former ones are more complex to produce. It is also interesting to observe that the size of the maximum pore tends to decrease with increasing staggering (NS → S → 2S) for the as-built specimens. The authors believe that this can be explained with the fact that the cell wall thickness increases with staggering by design and this appears to reduce the size of the pores.

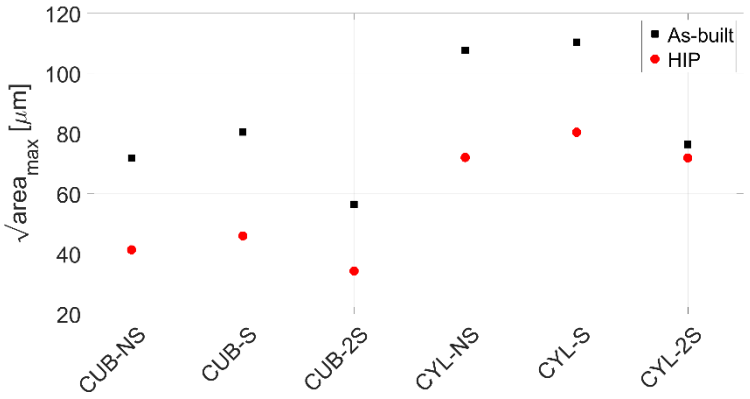

Figure 3. Maximum defect size.

3.2. CT dimensional evaluation

The structural analysis showed that significant structural distortions characterize the specimens, as depicted in Figure 4. The misalignment of the cell walls (consider the relative positions of the measured and CAD joint centers identified by the red and green point, respectively) can induce bending and shear actions that increase the severity of the tensions produced by the fatigue loading cycles. The increased severity of the notches of the real junction with respect to the CAD radius leading to higher local stresses can be also clearly observed.

In Figure 5, the CT measurement results of cell-wall diameters are shown for the HIPed structures. The staggered structures have shown a wider distribution of the cell-wall diameters, but the modal value of the wall diameter is closer to the nominal CAD value. In other words, the deviation from the CAD geometry is higher for the non-staggered structures.

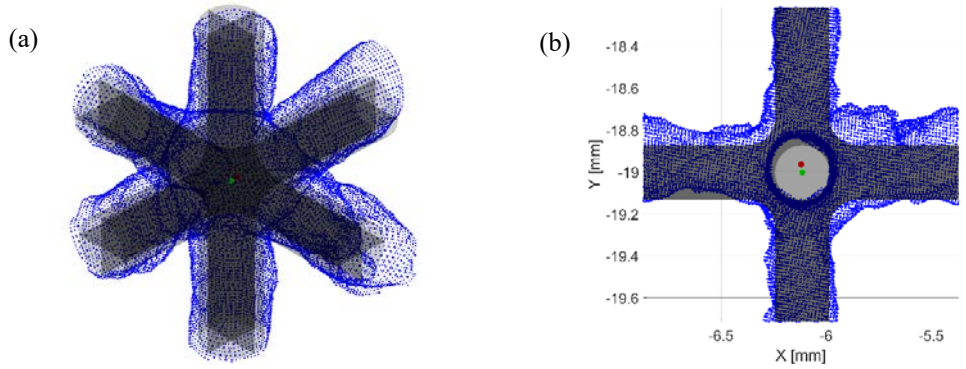

Figure 4. CT dimensional analysis results of the joints. Position of the measured joint center (red point, obtained by CT data) compared with the corresponding nominal center (green point) of specimen CUB-NS (HIPed). The black surface represents the CAD model and blue dots represent the measured surface. (a) 3D view; (b) projection on the XY plane (normal to the vertical strut in part (a)).

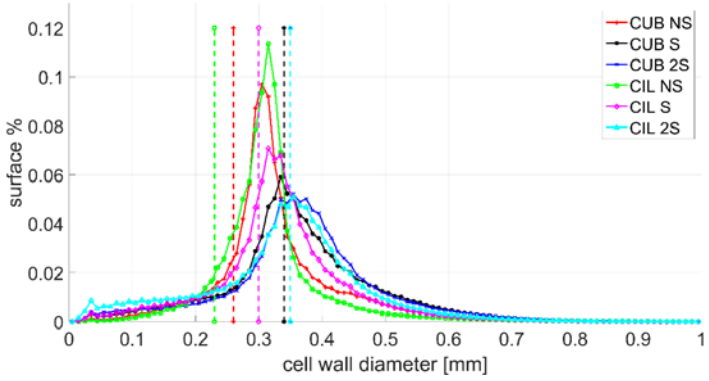

Figure 5. Cell-wall diameter distribution for the HIPed specimens (search angle 30°); the vertical lines represent the nominal CAD cell-wall diameters.

3.3. Residual stresses

Residual stresses were measured in an as-built CUB-NS specimen. Detrimental tensile residual stresses on the circumference (+200 ± 80 MPa) and in the axial direction (+100 ± 70 MPa) were found in the surface regions near scaffold junction in location 1. While in location 2 both tensile and compressive RS were present: $\sigma_x \approx +300 \pm 100$ MPa and $\sigma_y \approx -100 \pm 70$ MPa (see coordinates in Fig. 2d).

3.4. Fatigue resistance

The fatigue resistance at 10^6 cycles for each structure with its standard deviation is shown in Figure 6. HIPing does not appear to have a clear effect on the fatigue resistance. The most reasonable explanation for this is that fatigue resistance is controlled by the surface quality in terms of roughness and especially notches and not by the internal pores. In fact, the HIP treatment does not reduce the severity of notches but only the size of pores. On the other hand, the data also suggest that staggering has a positive effect on fatigue resistance and this effect is more marked in the cubic samples. The most likely explanation for this is based on the values of K_t calculated from the FE simulations (Table 2): the values of K_t in the staggered cubic specimens decrease remarkably because the cell wall thickness and the fillet radius both increase. The same does not apply to the cylindrical structures because of the more complicated design that causes a non-uniform distribution of loads on the transversal section of the staggered structures. Thus, some walls carry more load than others and the tensions are higher at the corresponding junctions despite the higher values of t_0 and R.

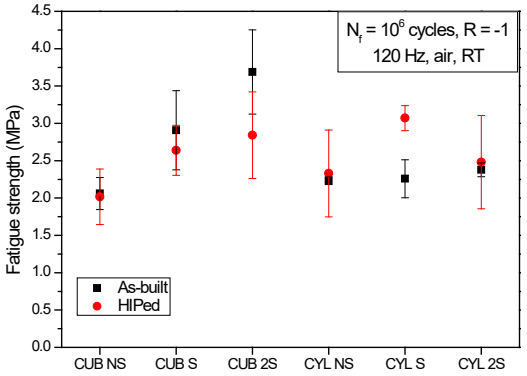

Figure 6. Fatigue resistance at 10^6 cycles.

The fatigue notch factors K_f could be computed because the fatigue resistance at 10^6 cycles of SLM unnotched bulk Ti6Al4V specimens was measured, both in the stress relieved and the HIPed conditions (Benedetti, 2017): $\sigma_{10^6}^{HIP} = 380$ MPa and $\sigma_{10^6}^{as-built} = 240$ MPa. Thus, we predicted K_t from the ideal geometry and K_f from the experimental data. Normally, fatigue notch factors are lower than K_t at long fatigue lives, Dowling (2013). Comparing the values reported in Table 2, K_f is higher than K_t. In our view, this indicates that the notches introduced in these structures due to the manufacturing process are more severe than what can be predicted from the CAD model.

Table 2. Stress concentration factor and fatigue notch factors for each structure.

Structure	K_t	K_f as-built	K_f HIPed
CUB-NS	62	115	188
CUB-S	49	82	144
CUB-2S	37	65	133
CYL-NS	58	107	163
CYL-S	59	105	123
CYL-2S	68	100	153

4. Conclusions

The manufacturing defects (internal porosity, structural distortions, dimensional deviations, residual stresses) in SLM cellular specimens were investigated by means of micro-Xray computed tomography and optical methods and the fully-reversed fatigue resistance at 10^6 cycles of the same specimens was measured. The possible effects of defects on fatigue resistance were discussed with the aid of FE analyses. In addition, the effect of HIPing on both the defectiveness and the fatigue resistance was evaluated. The HIPing treatment considerably reduces internal porosity, but it does not have a clear effect on fatigue resistance because fatigue resistance is not affected as much by internal porosity as by surface defects, especially sharp notches. Cellular structures designed with less fine geometrical details appear to be less affected by internal porosity. Residual stresses were measured on a very limited part of the specimen and thus the results can only prove that they can exist in the structure even after a stress relief heat treatment. This fact should warn the designer on the complexity of fatigue behavior of such structures. In addition, the fact that this kind of measurements are possible is an interesting result.

References

Ahmadi, S., M., Yavari, S., A., Wauthle, R., Pouran, B., Schrooten, J., Weinans, H., Zadpoor, A. A., 2015. Additively manufactured open-cell porous biomaterials made from six different space-filling unit cells: the mechanical and morphological properties, Materials 8, pp. 1871-1896

Benedetti, M., Torresani, E., Leoni, M., Fontanari, V., Bandini, M., Pederzolli, C., Potrich, C., 2017. The effect of post-sintering treatments on the fatigue and biological behavior of Ti- 6Al-4V ELI parts made by selective laser melting, J. Mech. Behav. Biomed. Mater. 71, pp. 295–306.

Beretta, S., Murakami, Y., 1998. Statistical analysis of defects for fatigue strength prediction and qualityt control of materials, Fatigue & Fracture of Engineering Materials & Structures 21, pp. 1049-106

De Chiffre, L., Carmignato, S., Kruth, J.-P., Schmitt, R., Weckenmann, A., 2014. Industrial applications of computed tomography. CIRP Annals Man. Tech., vol. 63(2), pp. 655-677

Dowling, N. E., 2013. Mechanical Behavior of Materials, Fourth Ed., Pearson

Kerckhofs, G. et al, 2008. Validation of x-ray microfocus computed tomography as an imaging tool for porous structures, Review of Scientific Instruments 79

Khademzadeh, S., Carmignato, S., Parvin, N., Zanini, F., Bariani P. F., 2016. Micro porosity analysis in additive manufactured NiTi parts using micro computed tomography and electron microscopy. Materials & Design, vol. 90, pp. 745-752

de Krijger, J., Rans, C., Van Hooreweder, B., Lietaert, K., Pouran, B., Zadpoor, A. A., 2016. Effects of applied stress ratio on the fatigue behavior of additively manufactured porous biomaterials under compressive loading, Journal of the mechanical behavior of biomedical materials

Leuders, S., Thoene, M., Riemer, A., Niendorf, T., Troester, T., Richard, H. A., Maier, H. J., 2013. On the mechanical behaviour of titanium alloy Ti6Al4V manufactured by selective laser melting: Fatigue resistance and crack growth perfirmance, International Journal of Fatigue 48, pp. 300-307

Long, M., Rack, H. J., 1998. Titanium alloys in total joint replacement – a materials science perspective, Biomaterials 19, pp. 1621-1639

Maxwell, D. C., Nicholas, T., 1999. A rapid method for generation of a Haigh diagram for high cycle fatigue, Fatigue and Fracture Mechanics: Twenty-Ninth Volume, ASTM STP 1332, Panontin T. L. and Sheppard S. D., Eds., American Society for Testing Materials, West Conshohocken, PA

Murakami, Y., 2002. Metal Fatigue: Effects of Small Defects and Nonmetallic Inclusions, Elsevier

Murr, L. E., Gaytan, S. M., Medina, F., Martinez, E., Martinez, J. L., Hernandez, D. H., Machado, B. I., Ramirez, D. A., Wicker, R. B., 2010. Characterization of Ti6Al4V open cellular foams fabricated by additive manufacturing using electron beam melting, Materials Science and Engineering A 527, pp. 1861-1868

Niinomi, M., 2008. Mechanical biocompatibilities of titanium alloys for biomedical applications, Journal of the Mechanical Behavior of Biomedical Materials I, pp. 30-42

Qiu, C., Adkins, N. J. E., Attallah, M. M., 2013. Microstructure and tensile properties of selectively laser-melted and HIPed laser-melted Ti6Al4V, Materials Science & Engineering A 578, pp. 230-239

Ryan, G., Pandit, A., Apatsidis, D. P., 2006. Fabrication methods of porous metals for use in Orthopaedic applications, Biomaterials 27, pp. 2651-2670

Schajer, G., Winiarski, B., Withers, P. J., Hole-drilling Residual Stress Measurement with Artifact Correction Using Full-field DIC Experimental Mechanics, 2013. 53(2): p. 255-265

Singh, R., Lee, P. D., Dashwood, R. J., Lindley, T. C., 2010. Titanium fomas for biomedical applications: a review, Materials Technology 25, No. 3/4

Tan, X. P., Tan, Y. J., Chow, C. S. L., Tor, S. B., Yeong, W. Y., 2017. Metallic powder-bed based 3D printing of cellular scaffolds for orthopaedic implants: A state-of-the-art review on manufacturing, topological design, mechanical properties and biocompatibility, Materials Science and Engineering C [In Press]

Van Hooreweder, B., Apers, Y., Lietaert, K., Kruth, J.-P., 2017. Improving the fatigue performance of porous metallic biomaterials produced by Selective Laser Melting, Acta Biomaterialia 47, pp. 193-202

Winiarski, B., Benedetti, M., Fontanari, V., Allahkarami, M., Hanan, J. C., Withers, P. J., 2016. High spatial resolution evaluation of residual stresses in shot peened specimens containing sharp and blunt notches by micro-hole drilling, micro-slot cutting and micro-X-ray diffraction methods, Experimental Mechanics 56, pp. 1449-1463

Winiarski, B., Schajer, G. S., Withers, P. J., 2012a. Surface Decoration for Improving the Accuracy of Displacement Measurements by Digital Image Correlation in SEM, Experimental Mechanics 52(7), pp. 793-804

Winiarski, B., Withers, P. J., 2012b. Micron-Scale Residual Stress Measurement by Micro-Hole Drilling and Digital Image Correlation, Experimental Mechanics 52(4), pp. 417-428

Wits, W. W. et al, 2016. Porosity testing methods for the quality assessment of selective laser melted parts, CIRP Annals Man. Tech. 65(1), pp. 201-204

Zargarian, A., Esfahanian, M., Kadkhodapour, J., Ziaei-Rad, S., 2016. Numerical simulation of the fatigue behavior of additive manufactured titanium porous lattice structures, Materials Science and Engineering C 60, pp. 339-347

Zhao, S., Li, S. J., Hou, W. T., Hao, Y. L., Yang, R., Murr, L. E., 2016a. Microstructure and mechanical properties of open cellular Ti6Al4V prototypes fabricated by electron beam melting for biomedical applications, Materials Technology: Advanced Performance Materials 31, No. 2

Zhao, X., Li, S., Zhang, M., Liu, Y., Serecombe, T. B., Wang, S., Hao, Y., Yang, R., Murr L. E., 2016b. Comparison of the microstructures and mechanical properties of Ti6Al4V fabricated by selective laser melting and electron beam melting, Materials and Design 95, pp. 21-31